PAPER

Check for updates

Dependence of defect structure on In concentration in InGaN epilayers grown on AlN/Si(111) substrate†

Arun Malla Chowdhury, ⓘ *ab Deependra Kumar Singh, ⓘ a Basanta Roul,ac K. K. Nanda*ade and S. B. Krupanidhi*a

InGaN epilayers with different indium concentrations have been grown on a 100-nm-thick AlN/n-Si(111) template using plasma assisted molecular beam epitaxy. The sample with the lowest indium (In) content is found to exhibit the highest crystallinity. Furthermore, the types as well as the densities of the threading dislocations in InGaN have been analyzed *via* high resolution X-ray diffraction measurements. The InGaN epilayers have been described as mosaic crystals, which are characterized by biaxial strain, hydrostatic strain, and mean tilt and twist angles. It is observed that the biaxial strain increases with increasing indium content and the hydrostatic strain decreases with increasing indium content in the films. The twist and tilt angles have also been correlated with the edge and screw dislocation densities, respectively. Furthermore, it has been concluded that point defects dominate in samples with a lower In content whereas trench defects and sub-interfacial extended defects dominate in samples with a higher In content.

Introduction

In recent years, InGaN-based devices have garnered tremendous research interest due to the possibility of extensive band gap engineering through modulation of the In-to-Ga ratio, thereby covering a large range of wavelengths. Therefore, InGaN epitaxial layers have shown high demands in optoelectronic devices such as light-emitting diodes (LEDs), lasers, optical communications and in photodetection.[1–9] However, the industrialization of InGaN-based devices with larger In contents still faces some challenges imposed by the inherent material properties.[10–13] Firstly, as the In content is increased, the mismatch to GaN also increases, which results in a higher strain in these ternary alloys.[14,15] Secondly, GaN and InN have a large difference in their thermal stabilities. InN starts to dissociate at ~ 500 °C,[16] which is well below the ideal growth temperature for GaN (~ 700 °C) in molecular beam epitaxy.[17] Hence, to achieve high In concentrations, the substrate temperature must be kept below 500 °C, which eventually reduces the mobility of Ga adatoms on the substrate surface. This leads to the formation of 3D islands, resulting in a high surface roughness along with an inhomogeneous composition in the alloy.[12,18–20] Moreover, at the temperatures typical for InGaN growth, the desorption rate of In is lower than the decomposition rate of In–N bonds, making the accumulation of In droplets on the substrate surface unavoidable.[21,22] The majority of InGaN ternary alloys are predicted to be thermodynamically unstable and show a tendency towards clustering and phase separation.[23] Therefore, a good-quality InGaN layer needs an appropriate substrate temperature along with proper In incorporation to avoid the phase separation. Therefore, it is very important to understand the strain and compositional effects in these ternary alloys, for improving device quality for a better performance.

However, extensive studies have been carried out for the growth of InGaN epilayers on a GaN buffer layer to obtain a better crystalline quality for solid-state lighting applications such as LEDs, laser diodes and photodetectors.[1,2,5,24,25] However, the GaN buffer layer does not meet the need for using the InGaN epilayer in broad band semiconductor–insulator–semiconductor (S–I–S) photodetection applications. For broad band S–I–S photodetector applications, it is required to have an insulating layer in between two semiconductors.[26,27] If we consider the insulating layer to be AlN from III-nitride materials, then it is necessary to understand the growth

a Materials Research Centre, Indian Institute of Science, Bangalore-560012, India. E-mail: nanda@iisc.ac.in, sbk@iisc.ac.in, amchowdhury@iisc.ac.in

b Department of Physics, Syamsundar College, University of Burdwan, East Bardhaman, West Bengal 713424, India

c Central Research Laboratory, Bharat Electronics, Bangalore 560013, India

d Institute of Physics, Bhubaneswar, Odisha – 751005, India

e Homi Bhabha National Institute, Mumbai, Maharashtra – 400094, India

† Electronic supplementary information (ESI) available: HRXRD scans of higher order symmetric and asymmetric planes and XPS spectra of the samples. See DOI: https://doi.org/10.1039/d2ma00438k

mechanism of the InGaN epilayer on AlN directly. Recently, Hu *et al.*[28] reported the application of LEDs using the AlN buffer layer, although that study shows the use of a GaN buffer layer on top of the AlN layer, and they did not grow the InGaN layer directly on the AlN layer. Therefore, it is necessary to understand the types of strain and defects present in the InGaN epilayers with different indium fractions on the AlN epilayer.

In this study, three InGaN epilayers with different indium concentrations have been grown on a 100-nm-thick AlN/n-Si(111) template using plasma assisted molecular beam epitaxy (PAMBE). It was important to check the qualities of the InGaN epitaxial layers with increasing indium content on the AlN template and the resulting mosaic structure characteristics such as the biaxial strain, hydrostatic strain, tilt angle, twist angle and dislocation densities, which were investigated *via* high-resolution X-ray diffraction measurements. Moreover, field emission microscopy, atomic force microscopy and photoluminescence measurements were also introduced to study the surface and optical properties. It was found that the biaxial strain increases with increasing indium content, and the hydrostatic strain decreases with increasing indium content in the films. Furthermore, it has been concluded that point defects dominate in lower indium content samples, and trench defects and sub-interfacial extended defects dominate in higher indium content samples.

Growth conditions, sample preparation and experimental details of InGaN epilayers

Three InGaN epitaxial layers with different indium fractions were grown using plasma assisted molecular beam epitaxy (PAMBE) on 100-nm-thick AlN/n-Si(111) templates. During the growth of sample A, the In and Ga effusion cell temperatures were kept at 770 °C and 880 °C, respectively, and the corresponding beam equivalent pressure (BEP) values were maintained at 1.69×10^{-7} and 1.26×10^{-7} mbar, respectively. On the other

hand, for samples B and C, the In effusion cell temperature was reduced to 750 °C and the corresponding BEP was maintained at 1.13×10^{-7} mbar. Moreover, the only difference in growth conditions between sample B and sample C is that Si doping was introduced in sample C and, consequently, a lower indium fraction (In $\approx$ 10%) in sample C was achieved compared with sample B (In $\approx$ 22%), and details of these doping mechanisms are described elsewhere.[26,29] Furthermore, the substrate temperature for all three samples was kept constant at 550 °C. The N_2 flow rate and plasma power for all three samples were kept constant at 1 SCCM and 350 W, respectively. During growth, the plasma pressure was maintained at 6×10^{-5} mbar and all samples were grown for 3 h without any intermediate steps. Structural characterization *via* strain and lattice constant measurements was carried out using a high-resolution X-ray diffractometer (HRXRD) (Bruker D8 discover) with CuKα1 (1.54056 Å) radiation. The thickness, surface morphologies and roughness of the films were characterised using field-emission scanning electron microscopy (FESEM) and atomic force microscopy (AFM).

Results and discussions

The HRXRD 2θ–ω scan in the (0002) direction and the full width at half maxima (FWHM) of samples A–C are presented in Fig. 1(a) and Fig. 1(b), respectively. All three samples (A–C) show strong peaks of the 0002 reflections along with the substrate peaks. It can be seen from Fig. 1(a) that sample A has a higher In concentration than samples B and C, and that sample B has a higher In concentration than that of sample C. The higher order 2θ–ω and rocking curve scans of the symmetric (0004) and (0006) planes are shown in Fig. S1 (ESI†). Similarly, the 2θ–ω and rocking curve scans of the asymmetric (105) and (205) planes for all three samples are shown in Fig. S2 (ESI†). Consequently, the 2θ peak values of the symmetric reflections of all three samples along with the (0002) reflections are presented in Table 1. This table also shows the FWHM values from rocking curve scans of the
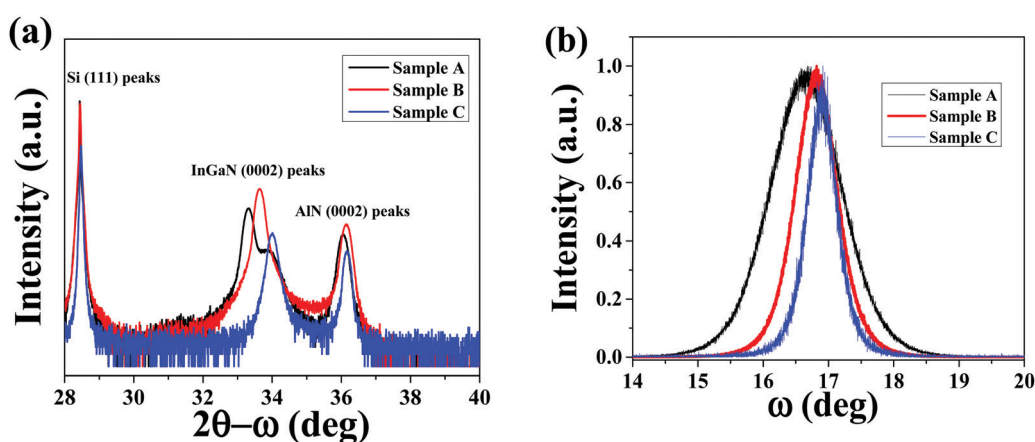

Fig. 1 (a) HRXRD scans of the InGaN epilayers along the (0002) plane. (b) Rocking curve measurements for the InGaN epilayers of the (0002) planes.

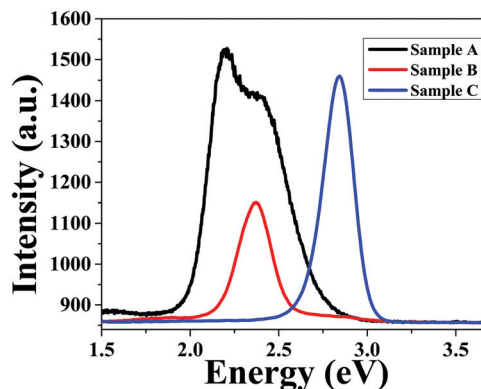**Table 1** Parameters obtained from symmetric HRXRD scans

	Symmetric planes	(0002)	(0004)	(0006)
Sample A	HRXRD peak position (2θ) in degrees	33.34	70.08	118.69
	FWHM (ω) in degrees	1.31	1.74	1.34
Sample B	HRXRD peak position (2θ) in degrees	33.65	70.65	120.44
	FWHM (ω) in degrees	0.77	1.05	0.97
Sample C	HRXRD peak position (2θ) in degrees	34.01	71.48	122.38
	FWHM (ω) in degrees	0.55	0.58	0.51

three samples corresponding to all reflections. Moreover, the values of the asymmetric reflections such as (105) and (205) for the three samples are presented in Table 2. The values of the inclination angles (χ) are displayed in Table 3 for the asymmetric planes.

It can be seen from Tables 1 and 2 that the FWHM values of sample C are smaller than those of sample A and sample B for every symmetric and asymmetric plane, which indicates the better crystalline quality of sample C. In addition, sample A shows the spinodal decomposition in the (0002) reflection, which is due to the presence of the higher indium content in sample A. This is also supported by photoluminescence (PL) measurements, which are shown in Fig. 2 for samples A–C.

The indium concentration for all the samples was calculated using Vegard's law.[26,29] The indium concentration values were found to be 26%, 22% and 10% for samples A, B, and C, respectively. The FESEM images of the top surface and cross-sectional views of samples A–C are shown in Fig. 3.

It can be seen that sample C, with the lower indium content, has a smooth and planar surface. On the other hand, a large number of pits can be observed in sample B, although the remaining surface shows a planar nature. By contrast, the FESEM image of sample A shows quite a rough surface compared with the other two samples. Furthermore, Fig. 3(a) suggests an initial 3D growth mechanism in the InGaN epilayer. Therefore, with increasing indium concentration, the growth mode gradually shifts from a 2D to 3D mode due to the increase

Table 2 Parameters obtained from asymmetric HRXRD scans

		(105)	(205)
Sample A	HRXRD peak position (2θ) in degrees	100.16	128.34
	FWHM (ω) in degrees	1.41	1.52
Sample B	HRXRD peak position 2θ) in degrees	101.36	130.05
	FWHM (ω) in degrees	1.02	1.418
Sample C	HRXRD peak position (2θ) in degrees	102.72	132.62
	FWHM (ω) in degrees	0.84	1.34

Table 3 Values of inclination angles of asymmetric planes

	Asymmetric planes	Inclination angle (χ) in degrees
Sample A	(105)	20.7693
	(205)	37.1804
Sample B	(105)	20.6635
	(205)	37.0266
Sample C	(105)	20.5337
	(205)	36.8374

Fig. 2 Photoluminescence spectra of InGaN epilayers.

in lattice mismatch with the underlying AlN layer. Similarly, the AFM images of samples A–C are shown in Fig. 4. The values of the thickness and surface roughness are displayed in Table 4.

The values in Table 4 indicate that the roughness of sample C is lower compared with the other samples. The low roughness and the smoother surface in sample C indicate that, due to the presence of the lower indium fraction, the degree of lattice crystalline quality is increased. It is well known that a higher indium fraction in the InGaN lattice decreases the quality of the InGaN epilayers and as well as greater defects and higher strain values being observed. On the other hand, it has been observed from the HRXRD, FESEM and AFM studies that the quality of sample A is very poor compared with samples B and C. Furthermore, sample A shows a split in the (0002) reflection, which could indicate either short-range spinodal decomposition or long-range phase separation, or simply the partial strain relaxation of some parts of the InGaN layer. Moreover, the short-range spinodal decomposition or long-range phase separation is also supported by the PL spectrum as shown in Fig. S3 (ESI†). Furthermore, it can be seen from Fig. S3 (ESI†) that sample A has a hump around 31.3 degrees in the HRXRD pattern, which is just the InN (0002) reflection peak in the sample. Hence, sample A is not suitable for opto-electronic device applications and was excluded from further analysis. We subsequently took samples B and C for further investigations such as XPS studies to verify the indium concentration, and the results are shown in Fig. S4 (ESI†).

The nature of the biaxial strain of the InGaN layer on the GaN layer has been reported in many studies,[30–33] but the behaviour with the AlN layer remains to be understood. Therefore, to further investigate the strain, stress and dislocation densities of these InGaN layers, further analysis was carried out using the HRXRD data. The in-pane and out-of-plane lattice parameters a and c, respectively, were determined using the following relationship for the hexagonal system[34]

$$\frac{1}{d_{hkl}^2} = \frac{l^2}{c^2} + \frac{4}{3}\left(\frac{h^2 + hk + k^2}{a^2}\right) \quad (1)$$

where d_{hkl} is the interplanar spacing between two planes. Values of d_{hkl} were measured using Bragg's law, taking the higher order
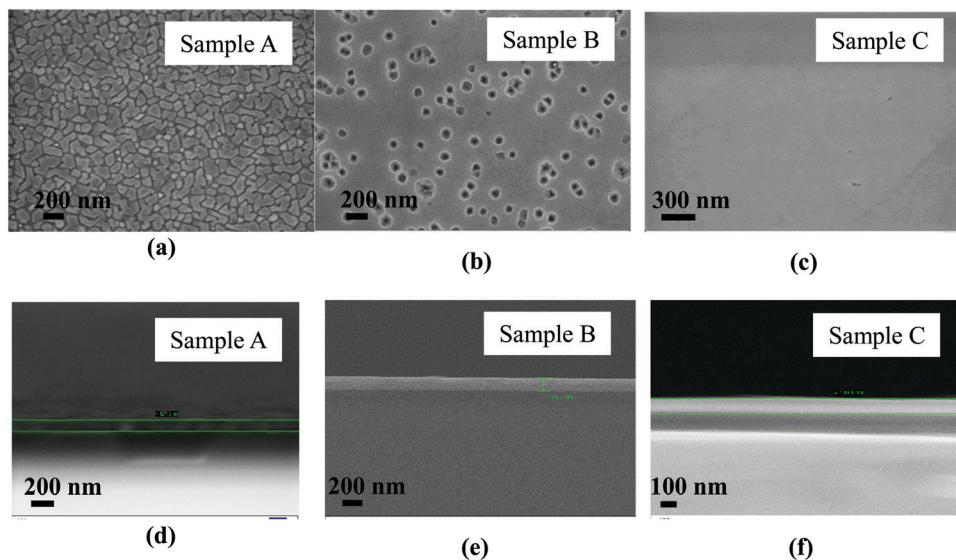
Fig. 3 Top surface FESEM images of (a) sample A, (b) sample B, and (c) Sample C. (d) Cross-sectional FESEM images of sample A, (e) sample B, and (f) sample C. Parts b, c, e and f are reproduced with permission from ref. 29.
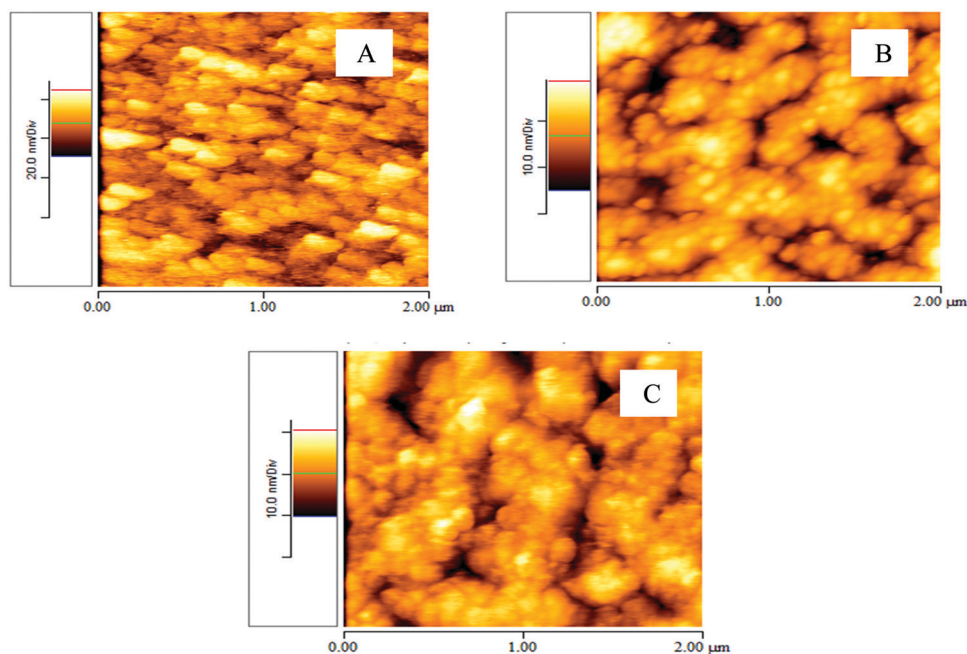

Fig. 4 AFM images of (A) sample A, (B) sample B, and (C) sample C. Parts B and C are reproduced with permission from ref. 29.

reflections such as d_{004}, d_{006} for the symmetric planes and d_{105}, d_{205} for the asymmetric planes. Moreover, the in-plane and out-of-plane strain, ε_a and ε_c, respectively, can be described as

$$\varepsilon_a = \frac{a - a_0}{a_0} \tag{2}$$

$$\varepsilon_c = \frac{c - c_0}{c_0} \tag{3}$$

where a_0 and c_0 are the relaxed lattice parameters for the InGaN epilayers. The relaxed lattice parameters were obtained using Vegard's law, which is given as

Table 4 Values obtained from FESEM and AFM measurements

	Thickness from FESEM cross-section (nm)	AFM rms roughness (nm)
Sample A	127	5
Sample B	150	3.8
Sample C	110	3.2

$$c_0 = (1-x)c_0^{GaN} + c_0^{InN} \tag{4}$$

$$a_0 = (1-x)a_0^{GaN} + a_0^{InN} \tag{5}$$

where x is the indium fraction, c_0^{GaN} and a_0^{GaN} are the strain-free lattice parameters for GaN, and c_0^{InN} and a_0^{InN} are the strain-free lattice parameters for InN.[13]

However, InGaN layers grown using the MBE technique contain a lot of defects and dislocation densities due to several reasons, such as doping, lattice mismatch and the different thermal expansion coefficient from the underneath substrate layer. Because of these reasons there could be contraction and expansion in the lattice constants, which leads to biaxial compressive or tensile strain in the layer. Furthermore, the measured in-plane (ε_a) and out-of-plane (ε_c) strain comprises two components, one is biaxial strain, and the other is hydrostatic strain. These are given by the following equations as[34,35]

$$\varepsilon_a = \varepsilon_a^{(bi)} + \varepsilon_{hy} \tag{6}$$

$$\varepsilon_c = \varepsilon_c^{(bi)} + \varepsilon_{hy} \tag{7}$$

where $\varepsilon_a^{(bi)}$ and $\varepsilon_c^{(bi)}$ are the in-plane and out-of-plane biaxial strain, respectively. The parameter ε_{hy} is the hydrostatic strain, which is described by the following equation[34,35]

$$\varepsilon_{hy} = \frac{1-\nu}{1+\nu}\left(\varepsilon_c + \frac{2\nu}{1-\nu}\varepsilon_a\right) \tag{8}$$

$$\nu = \frac{c_{13}}{c_{13}+c_{33}} \tag{9}$$

where ν is the Poisson ratio and c_{13} and c_{33} are the elastic constants of the InGaN layers. The values of the elastic constants were obtained from Vegard's law, which is described by the following relations:

$$c_{13} = (1-x)c_{13}^{GaN} + xc_{13}^{InN} \tag{10}$$

$$c_{33} = (1-x)c_{33}^{GaN} + xc_{33}^{InN} \tag{11}$$

where c_{13}^{GaN} and c_{33}^{GaN} are the elastic constants of bulk GaN, and c_{13}^{InN} and c_{33}^{InN} are the elastic constants of bulk InN.[13]

The values of the in-plane stress (σ_{in}) can be derived in terms of the biaxial strain and elastic constants and are given by[34,35]

$$\sigma_{in} = \left[c_{11} + c_{12} - 2\frac{c_{13}^2}{c_{33}}\right]\varepsilon_a^{(bi)} \tag{12}$$

where c_{11} and c_{12} are the elastic constants of the corresponding InGaN layers, and the obtained values are discussed in terms of the relations below given:

$$c_{11} = (1-x)c_{11}^{GaN} + xc_{11}^{InN} \tag{13}$$

$$c_{12} = (1-x)c_{12}^{GaN} + xc_{12}^{InN} \tag{14}$$

where c_{11}^{GaN} and c_{12}^{GaN} are the elastic constants of bulk GaN, and c_{11}^{InN} and c_{12}^{InN} are the elastic constants of bulk InN.[36] The values of the characteristic parameters for the samples are presented in Table 5.

Generally, biaxial strain in the epilayers appeared due to lattice mismatch and the different lattice expansion coefficients between the sample layer and the substrate, but on the other

Table 5 Characteristic parameters for all the InGaN samples

	Sample B	Sample C
c (Å)	5.3266	5.2747
a (Å)	3.2432	3.2126
c_0 (Å)	5.2990	5.2368
a_0 (Å)	3.2659	3.2241
ε_a	-6.9506×10^{-3}	-3.567×10^{-3}
ε_c	5.208×10^{-3}	7.237×10^{-3}
$\varepsilon_a^{(bi)}$	-7.839×10^{-3}	-7.083×10^{-3}
$\varepsilon_c^{(bi)}$	4.3196×10^{-3}	3.721×10^{-3}
ε_{hy}	8.884×10^{-4}	3.516×10^{-3}
ν	0.216	0.208
c_{13} (GPa)	100.58	101.9
c_{33} (GPa)	365.18	386.9
c_{11} (GPa)	335.32	352.6
c_{12} (GPa)	130.6	133
σ_{in} (GPa)	-3.218	-3.059

hand, hydrostatic strain in the layer appeared due to the doping and defects.[34,35] It is seen from Table 5 that, for the samples, the values of the measured in-plane stain (ε_a) and the biaxial strain ($\varepsilon_a^{(bi)}$) are negative in nature; therefore, it can be suggested that the in-plane strain values are compressive in nature, i.e., the in-plane lattice constants are decreased from the relaxed lattice constants. Consequently, the values of the out-of-plane strain parameters (ε_c, $\varepsilon_c^{(bi)}$) are positive in nature, i.e., the out-of-plane lattice constants are increased from the relaxed values. This behaviour of the lattice constants changed the hexagonal unit cell from its relaxed condition, and is depicted in Fig. 5. It is found that the biaxial strain value in samples B and C increases (greater negative value) with increasing indium content in the InGaN epilayer. There have been various literature reports that the in-plane strain increases with increasing indium fraction in InGaN lattices.[28,30,37–40] Hence, we can expect that the number of defects will also be enhanced with increasing in-plane strain as well as with increasing indium content. Moreover, the reason behind the increasing number of defects is that the increased strain in any layer must be relaxed to minimize the formation energy by some means, and defects are the best possible way to relax the high strain in an any epilayer, which is why if an epilayer contains a high level of strain then there is a high probability of a large number of defects present in that material to minimize the formation energy. Furthermore, several types of defects, such as V-type defects, trench defects and sub-interfacial extended-type defects, can appear due to the higher indium content and biaxial compressive strain in the material. However, recent studies have suggested that V-type defects are mostly kinetically driven and cannot be related to the higher indium content and with biaxial compressive strain.[15,41–43] On the other hand, it has been suggested that trench defects and sub-interfacial extended-type defects can be related to a higher indium content and as well as to biaxial compressive strain.[15,41,42,44] But some reports still suggest the dependency of V-type defects on a higher indium content and as well as on compressive strain.[37,39,45] In our FESEM results also (Fig. 3), it can be seen that there is no sign of V-pits in sample C, but as the In fraction is increased the V-type pits are observed in sample B. Therefore, the dependency of V-type defects on the indium fraction is still a
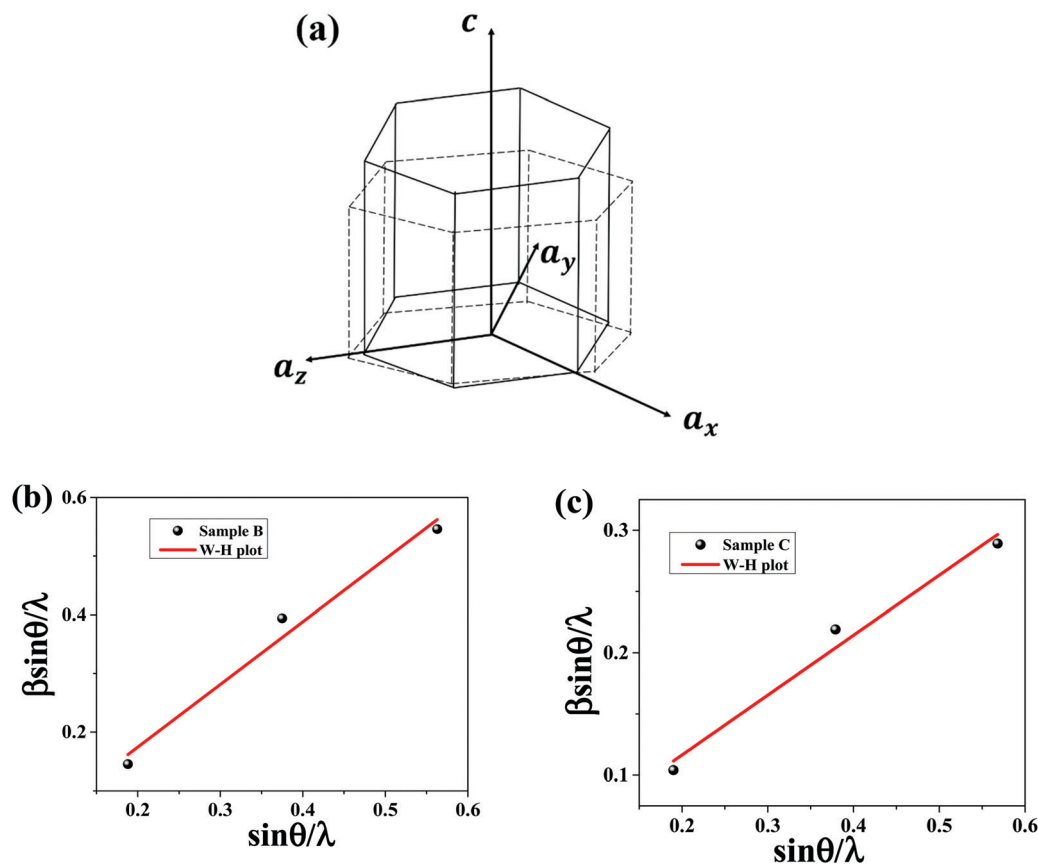
Fig. 5 (a) Schematic of a hexagonal unit cell under relaxed and strain conditions. (b) W–H plot for sample B, and (c) W–H plot for sample C.

matter of debate. On the other hand, the large difference between the covalent radii of In (r_{In} = 0.144 nm), Ga (r_{Ga} = 0.126 nm) and N (r_N = 0.07 nm) could be the reason for the high in-plane compressive strain in the samples with increasing indium content, although by contrast, it can be seen that the hydrostatic strain decreases with increasing indium content. It has already been discussed that the hydrostatic strain originates due to doping and defects such as point defects.[34,35] There are several types of point defect present in InGaN lattices, such as substitutional defects (In$_{Ga}$, In$_N$, Ga$_N$, N$_{Ga}$), interstitial defects (In$_i$, Ga$_i$, N$_i$) and vacancy-type defects (V_{In}, V_{Ga}, V_N). Now, the hydrostatic strain depends on the measured in-plane (ε_a) and out-of-plane (ε_c) strain, as shown in eqn (8). The value of ε_a increases with increasing indium content but the value of ε_c decreases with increasing indium content (Table 5). Therefore, the influence of the out-of-plane strain (ε_c) dominates over the in-plane strain (ε_a) in the case of hydrostatic strain (ε_{hy}) for the InGaN layers grown on AlN templates. Hence, in this present case, it can be stated that ε_c is a measure of point defects in the InGaN epilayers. Thus, it can be said that biaxial strain due to trench defects and sub-interfacial extended-type defects in the InGaN lattices increased with increasing indium fraction, and that hydrostatic strain due to point-type defects in the InGaN lattices decreased with increasing indium fraction. Therefore, we suggest that, in our case, point-type defects dominate in the lower indium fraction sample C and trench or sub-interfacial extended-type defects dominate in the

higher indium fraction sample B. Moreover, values of the in-plane stress (σ_{in}) were calculated using eqn (12) for all three samples. In the samples it is seen that the value of the in-plane stress increases with increasing indium content in a similar way as the in-plane biaxial strain increases, and this is to be expected because the in-plane stress is directly proportional to the in-plane biaxial strain of the sample (eqn (12)).

Next, the mosaic structure of the InGaN films was investigated *via* HRXRD rocking curve experiments, *i.e.*, ω scan measurements. Due to the large lattice mismatch between InGaN and the AlN template layer, a number of misoriented islands or sub-grains form at the heterostructure interface, giving rise to a mosaic structure. Therefore, the angle due to the out-of-plane rotation of these islands with respect to the surface normal is known as the tilt angle and, similarly, the angle due to the in-plane rotation with respect to the surface normal is known as the twist angle. Consequently, threading dislocation densities (TDs) become introduced by the process of coalescence at the heterojunction to bring close the misoriented sub-grains and, as a result, TDs become a strong measure of the mosaic structure in InGaN lattices.[46–49] Values of the tilt and twist angles can be calculated from the FWHM values of the symmetric and asymmetric planes, respectively.[34,46–48] However, to calculate precisely the tilt angle from symmetric planes, it is convenient to use the Williamson–Hall (W–H) plot. The plot of ($\beta \sin\theta/\lambda$) *vs.* ($\sin\theta/\lambda$) is known as the W–H plot, where β is the FWHM of each symmetric reflection

Table 6 Values of tilt, twist, screw and edge threading dislocation densities for InGaN samples

	β_{tilt}	β_{twist}	ρ_{screw} (cm^{-2})	ρ_{edge} (cm^{-2})
Sample B	1.069	1.418	9.26×10^{13}	4.39×10^{14}
Sample C	0.489	1.34	1.97×10^{13}	3.99×10^{14}

(0002, 0004, 0006) and θ is the Bragg angle and λ is the wavelength of the X-ray source. The W–H plot gives a straight line, and from the slope of the straight line the tilt angle can be evaluated, and the intercept with the y-axis gives the lateral coherence length. The W–H plots for samples B and C are shown in Fig. 5. On the other hand, the twist angle can be calculated by plotting the FWHM data of the asymmetric reflections (10 × 5, 20 × 5, 20 × 4, *etc.*) with the inclination angle χ, and with suitable fitting, the angle that is derived at $\chi = 90°$ can be considered as the twist angle. But in our case, obtaining the peaks for the asymmetric reflection planes greater than $\chi = 40°$ was very difficult. This might be because of the quality of the InGaN epilayers that were grown directly on the AlN layer, which had a large lattice mismatch. So far, preferably, most of the InGaN layers were grown either on a GaN epilayer or on a GaN buffer layer to obtain a high crystalline quality and also to obtain a reduced lattice mismatch compared with AlN. Therefore, we considered the FWHM values as the twist angle, which were derived at the largest possible inclination angle, as also suggested by Heinke *et al.*[50] In our present case, we took the FWHM values of 20 × 5 reflections as the twist angle and the corresponding inclination angles varied from $\chi = 37°$ to $\chi = 40°$ for all three samples. Hence, after evaluating the tilt and twist angles, the TDs can be calculated as they are directly proportional to the tilt and twist angles according to the expressions given below, where these equations are for random distributions of dislocation densities:[34,45,47]

$$\rho_{\text{screw}} = \frac{\beta_{\text{tilt}}^2}{4.35 b_{\text{screw}}^2} \qquad (15)$$

$$\rho_{\text{edge}} = \frac{\beta_{\text{twist}}^2}{4.35 b_{\text{edge}}^2} \qquad (16)$$

Here, ρ_{screw} and ρ_{edge} are the screw and edge dislocation densities, respectively, β_{tilt} and β_{twist} are the tilt and twist angles respectively, b_{screw} is the Burgers vector along [0001] and b_{edge} is the Burgers

vectors along $\frac{1}{3}[11\bar{2}0]$. The obtained values of β_{tilt}, β_{twist}, ρ_{screw} and ρ_{edge} are presented in Table 6.

It is seen that edge TDs are greater compared with screw TDs for both samples B and C. Furthermore, both TDs were increased with increasing indium content, indicating the greater number of defects and the decreasing crystalline quality with increasing indium fraction. Moreover, the obtained results of TDs are in good agreement with the strain calculations as well as the FESEM and AFM measurements with increasing indium content. We also carried out asymmetric reciprocal space mapping (RSM) to verify the defect densities, which is represented in Fig. 6. From the asymmetric RSM images, it can be observed that sample C has the lesser mosaicity and compositional inhomogeneity compared with sample B, as the RSM of sample C is highly symmetric compared with sample B. Therefore, it may be noted that the calculated defect densities in Table 6 are well supported by the RSM results.

Hence, it is seen from the above extensive calculations that the growth of the InGaN epilayer directly on a 100-nm-thick AlN layer shows good results in terms of the crystalline quality, despite of having a large lattice mismatch. In particular, for sample B, it is observed that despite having a moderately large indium fraction (In ≈ 22%) compared with sample C (In ≈ 10%), sample B still shows a good crystalline quality for future device applications, such as green LEDs, visible-range photo-detectors, *etc.* Furthermore, sample B needs extensive future research on the green gap issue in LED devices. On the other hand, sample C is the better candidate for Si-based S–I–S photodetection applications in the broad band range. It is necessary to have a good-quality InGaN layer on the AlN epilayer, which has been achieved by sample C.[26] Therefore, we suggest that a good quality of InGaN epilayers can also be achieved with different indium concentrations on an AlN epilayer, despite having large a lattice mismatch, and this work opens up a new research area of growing InGaN epilayers on AlN templates for future device applications.

Conclusion

In conclusion, InGaN epilayers with different In concentrations have been grown on AlN/Si(111), and it has been observed that
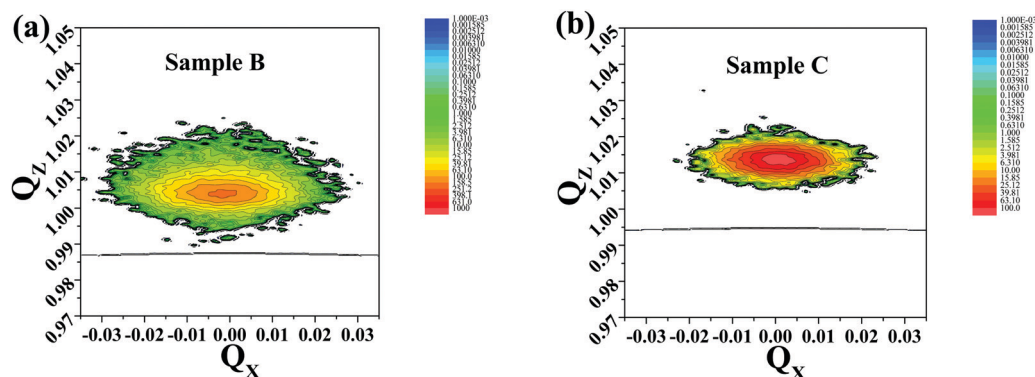
Fig. 6 Reciprocal space map around the (105) reflection for (a) sample B and (b) sample C. Q_x and Q_z are the reciprocal space vectors in Å^{-1}.

the crystalline and optical quality of the InGaN layers increases with decreasing In content. Extensive high-resolution X-ray diffraction measurements have been performed to calculate the various mosaic characteristics, such as the bi-axial strain, hydrostatic strain, stress and threading dislocation densities. A fundamental correlation between the tilt and twist angles has been established. This work opens up a new avenue to growing high-quality InGaN epilayers on AlN for future optoelectronic device applications.

Author contributions

Prof. S. B. Krupanidhi, Prof. K. K. Nanda and A. M. C. generated the idea and designed experiments. A. M. C. performed experiments. A. M. C., D. K. S. and B. R. prepared the manuscript. All authors participated in the discussion of experimental results and revision of the manuscript.

Conflicts of interest

There are no conflicts of interest to declare.

Acknowledgements

References

1 F. A. Ponce and D. P. Bour, Nitride-Based Semiconductors for Blue and Green Light-Emitting Devices, *Nature*, 1997, **386**(6623), 351–359.

2 Z. L. Li, P. T. Lai and H. W. Choi, A Reliability Study on Green InGaN-GaN Light-Emitting Diodes, *IEEE Photonics Technol. Lett.*, 2009, **21**(19), 1429–1431.

3 I. Akasaki, Fascinating Journeys into Blue Light (Nobel Lecture), *Ann. Phys.*, 2015, **527**(5–6), 311–326.

4 R. Dahal, B. Pantha, J. Li, J. Y. Lin and H. X. Jiang, InGaN/GaN Multiple Quantum Well Solar Cells with Long Operating Wavelengths, *Appl. Phys. Lett.*, 2009, **94**(6), 2007–2010.

5 K. Zhang, H. Liang, D. Wang, R. Shen, W. Guo, Q. Deng, Y. Liu, X. Xia, Y. Luo and G. Du, The Properties of Reversed Polarization Yellow InGaN-GaN MQWs in p-Side down Structure Grown by Metal-Organic Chemical Vapor Deposition on Sapphire Substrate, *Phys. E*, 2014, **64**, 57–62.

6 J. Liu, H. Liang, X. Xia, Y. Liu, J. Liu, Q. Abbas, R. Shen, Y. Luo, Y. Zhang and G. Du, Indium Incorporation Induced Morphological Evolution and Strain Relaxation of High Indium Content InGaN Epilayers Grown by Metal-Organic Chemical Vapor Deposition, *Cryst. Growth Des.*, 2017, **17**(6), 3411–3418.

7 E. Matioli, C. Neufeld, M. Iza, S. C. Cruz, A. A. Al-Heji, X. Chen, R. M. Farrell, S. Keller, S. DenBaars and U. Mishra, *et al.*, High Internal and External Quantum Efficiency InGaN/GaN Solar Cells, *Appl. Phys. Lett.*, 2011, **98**(2), 2009–2012.

8 A. M. Chowdhury, D. K. Singh, B. Roul, K. K. Nanda and S. B. Krupanidhi, Overcoming the Challenges Associated with the InN/InGaN Heterostructure via a Nanostructuring Approach for Broad Band Photodetection, *ACS Appl. Electron. Mater*, 2021, **3**(9), 4243–4253.

9 T. Walther, H. Amari, I. M. Ross, T. Wang and A. G. Cullis, Lattice Resolved Annular Dark-Field Scanning Transmission Electron Microscopy of (Al, In)GaN/GaN Layers for Measuring Segregation with Sub-Monolayer Precision, *J. Mater. Sci.*, 2013, **48**(7), 2883–2892.

10 E. Arslan and M. K. Ozturk, Evolution of the Mosaic Structure in InGaN Layer Grown on a Thick GaN Template and Sapphire Substrate, *J. Mater. Sci.: Mater. Electron.*, 2013, **24**(11), 4471–4481.

11 O. Ambacher, Growth and Applications of Group III-Nitrides, *J. Phys. D: Appl. Phys.*, 1998, **31**(20), 2653.

12 F. K. Yam and Z. Hassan, InGaN: An Overview of the Growth Kinetics, Physical Properties and Emission Mechanisms, *Superlattices Microstruct.*, 2008, **43**(1), 1–23.

13 S. Pereira, M. R. Correia, E. Pereira, K. P. O'Donnell, E. Alves, A. D. Sequeira, N. Franco, I. M. Watson and C. J. Deatcher, Strain and Composition Distributions in Wurtzite InGaN/GaN Layers Extracted from X-Ray Reciprocal Space Mapping, *Appl. Phys. Lett.*, 2002, **80**(21), 3913–3915.

14 I. H. Ho and G. B. Stringfellow, Solid Phase Immiscibility in GaInN, *Appl. Phys. Lett.*, 1996, **69**(18), 2701–2703.

15 S. L. Rhode, W. Y. Fu, M. A. Moram, F. C.-P. Massabuau, M. J. Kappers, C. McAleese, F. Oehler, C. J. Humphreys and R. O. Dusane, and S. S. Structure and Strain Relaxation Effects of Defects in $In_xGa_{1-x}N$ Epilayers, *J. Appl. Phys.*, 2014, **116**(10), 103513.

16 Q. Guo, O. Kato and A. Yoshida, Thermal Stability of Indium Nitride Single Crystal Films, *J. Appl. Phys.*, 1993, **73**(11), 7969–7971.

17 M. Kumar, B. Roul, T. N. Bhat, M. K. Rajpalke, P. Misra, L. M. Kukreja, N. Sinha, A. T. Kalghatgi and S. B. Krupanidhi, Improved Growth of GaN Layers on Ultra Thin Silicon Nitride/Si (1 1 1) by RF-MBE, *Mater. Res. Bull.*, 2010, **45**(11), 1581–1585.

18 Y. Zhang, X. Zhou, S. Xu, Z. Wang, Z. Chen, J. Zhang, J. Zhang and Y. Hao, Effects of Growth Temperature on the Properties of InGaN Channel Heterostructures Grown by Pulsed Metal Organic Chemical Vapor Deposition, *AIP Adv.*, 2015, **5**, 12.

19 A. Senichev, B. Dzuba, T. Nguyen, Y. Cao, M. A. Capano, M. J. Manfra and O. Malis, Impact of Growth Conditions and Strain on Indium Incorporation in Non-Polar m-Plane (10 1̄ 0) InGaN Grown by Plasma-Assisted Molecular Beam Epitaxy, *APL Mater.*, 2019, **7**, 12.

20 Y. S. Chen, C. H. Liao, C. T. Kuo, R. C. C. Tsiang and H. C. Wang, Indium Droplet Formation in InGaN Thin Films with Single and Double Heterojunctions Prepared by MOCVD, *Nanoscale Res. Lett.*, 2014, **9**(1), 1–12.

21 R. Kour, S. Arya, S. Verma, A. Singh, P. Mahajan and A. Khosla, Review—Recent Advances and Challenges in Indium Gallium Nitride (In$_x$Ga$_{1-x}$N) Materials for Solid State Lighting, *ECS J. Solid State Sci. Technol.*, 2020, **9**(1), 015011.

22 N. Sinha, B. Roul, S. Mukundan, G. Chandan, L. Mohan, V. M. Jali and S. B. Krupanidhi, Growth and Electrical Transport Properties of InGaN/GaN Heterostructures Grown by PAMBE, *Mater. Res. Bull.*, 2014, **61**, 539–543.

23 H. Morkoç and H. Morkoç, *Handbook of Nitride Semiconductors and Devices*, Wiley-VCH, 2008.

24 C. A. M. Fabien, A. Maros, C. B. Honsberg and W. A. Doolittle, III-Nitride Double-Heterojunction Solar Cells with High In-Content InGaN Absorbing Layers: Comparison of Large-Area and Small-Area Devices, *IEEE J. Photovoltaics*, 2016, **6**(2), 460–464.

25 Q. Zheng, M. Peng, Z. Liu, S. Li, R. Han, H. Ouyang, Y. Fan, C. Pan, W. Hu and J. Zhai, *et al.*, Dynamic Real-Time Imaging of Living Cell Traction Force by Piezo-Phototronic Light Nano-Antenna Array, *Sci. Adv.*, 2021, **7**(22), 1–9.

26 A. M. Chowdhury, G. Chandan, R. Pant, B. Roul, D. K. Singh, K. K. Nanda and S. B. Krupanidhi, Self-Powered, Broad Band, and Ultrafast InGaN-Based Photodetector, *ACS Appl. Mater. Interfaces*, 2019, **11**(10), 10418–10425.

27 A. M. Chowdhury, R. Pant, B. Roul, D. K. Singh, K. K. Nanda and S. B. Krupanidhi, Double Gaussian Distribution of Barrier Heights and Self-Powered Infrared Photoresponse of InN/AlN/Si(111) Heterostructure, *J. Appl. Phys.*, 2019, **126**(2), 025301.

28 H. Hu, S. Zhou, H. Wan, X. Liu, N. Li and H. Xu, Effect of Strain Relaxation on Performance of InGaN/GaN Green LEDs Grown on 4-Inch Sapphire Substrate with Sputtered AlN Nucleation Layer, *Sci. Rep.*, 2019, **9**(1), 1–9.

29 A. M. Chowdhury, B. Roul, D. K. Singh, R. Pant, K. K. Nanda and S. B. Krupanidhi, Temperature Dependent "S-Shaped" Photoluminescence Behavior of InGaN Nanolayers: Optoelectronic Implications in Harsh Environment, *ACS Appl. Nano Mater.*, 2020, **3**(8), 8453–8460.

30 L. Görgens, O. Ambacher, M. Stutzmann, C. Miskys, F. Scholz and J. Off, Characterization of InGaN Thin Films Using High-Resolution X-Ray Diffraction, *Appl. Phys. Lett.*, 2000, **76**(5), 577–579.

31 M. D. McCluskey, Van de Walle, C. G. Romano, L. T. Krusor and B. S. Johnson, N. M. Effect of Composition on the Band Gap of Strained In$_x$Ga$_{1-x}$N Alloys, *J. Appl. Phys.*, 2003, **93**(7), 4340–4342.

32 T. Böttcher, S. Einfeldt, V. Kirchner, S. Figge, H. Heinke, D. Hommel, H. Selke and P. L. Ryder, Incorporation of Indium during Molecular Beam Epitaxy of InGaN, *Appl. Phys. Lett.*, 1998, **73**(22), 3232–3234.

33 F. A. Ponce, S. Srinivasan, A. Bell, L. Geng, R. Liu, M. Stevens, J. Cai, H. Omiya, H. Marui and S. Tanaka, Microstructure and Electronic Properties of InGaN Alloys, *Phys. Status Solidi*, 2003, **240**(2), 273–284.

34 M. A. Moram and M. E. Vickers, X-ray Diffraction of III-Nitrides, *Reports Prog. Phys.*, 2009, **72**(3), 036502.

35 V. S. Harutyunyan, A. P. Aivazyan, E. R. Weber, Y. Kim, Y. Park and S. G. Subramanya, High-Resolution X-ray Diffraction Strain – Stress Analysis of GaN/Sapphire Heterostructures, *J. Phys. D. Appl. Phys.*, 2001, **34**(10A), A35.

36 A. F. Elastic Wright, Properties of Zinc-Blende and Wurtzite AlN, GaN, and InN, *J. Appl. Phys.*, 1997, **82**(6), 2833–2839.

37 T. L. Song, Strain Relaxation Due to V-Pit Formation in In XGa 1-XN/GaN Epilayers Grown on Sapphire, *J. Appl. Phys.*, 2005, **98**(8), 084906.

38 L. T. Romano, B. S. Krusor, M. D. McCluskey, D. P. Bour and K. Nauka, Structural and Optical Properties of Pseudomorphic InxGa1-XN Alloys, *Appl. Phys. Lett.*, 1998, **73**(13), 1757–1759.

39 C. Bazioti, E. Papadomanolaki, T. Kehagias, T. Walther, J. Smalc-Koziorowska, E. Pavlidou, P. Komninou, T. Karakostas, E. Iliopoulos and G. P. Dimitrakopulos, Defects, Strain Relaxation, and Compositional Grading in High Indium Content InGaN Epilayers Grown by Molecular Beam Epitaxy, *J. Appl. Phys.*, 2015, **118**, 15.

40 S. Pearton, GAN and ZNO-Based Materials and Devices, *Springer Ser. Mater. Sci*, 2012, **156**, 1.

41 S. L. Sahonta, M. J. Kappers, D. Zhu, T. J. Puchtler, T. Zhu, S. E. Bennett, C. J. Humphreys and R. A. Oliver, Properties of trench defects in InGaN/GaN quantum well structures, *Phys. Status Solidi A*, 2013, **210**(1), 195–198.

42 J. Bruckbauer, P. R. Edwards, T. Wang and R. W. Martin, High Resolution Cathodoluminescence Hyperspectral Imaging of Surface Features in InGaN/GaN Multiple Quantum Well Structures, *Appl. Phys. Lett.*, 2011, **98**(14), 141908.

43 J. Gruber, X. W. Zhou, R. E. Jones, S. R. Lee and G. J. Tucker, Molecular Dynamics Studies of Defect Formation during Heteroepitaxial Growth of InGaN Alloys on (0001) GaN Surfaces, *J. Appl. Phys.*, 2017, **121**(19), 195301.

44 F. C.-P. Massabuau, S.-L. Sahonta, L. Trinh-Xuan, S. Rhode, T. J. Puchtler, M. J. Kappers and C. J. Humphreys, and R. A. O. Morphological, Structural, and Emission Characterization of Trench Defects in InGaN/GaN Quantum Well Structures, *Appl. Phys. Lett.*, 2012, **101**(21), 212107.

45 D. Won, X. Weng and J. M. Redwing, Effect of Indium Surfactant on Stress Relaxation by V-Defect Formation in GaN Epilayers Grown by Metalorganic Chemical Vapor Deposition, *J. Appl. Phys.*, 2010, **108**, 9.

46 M. E. Vickers, M. J. Kappers, R. Datta, C. McAleese, T. M. Smeeton, F. D. G. Rayment and C. J. Humphreys, In-Plane Imperfections in GaN Studied by X-ray Diffraction, *J. Phys. D: Appl. Phys.*, 2005, **38**(10A), A99.

47 S. Christiansen, M. Albrecht and H. P. Strunk, Defect Structure of Epitaxial GaN Films Determined by Transmission Electron Microscopy and Triple-Axis X-Ray Diffractometry, *Philos. Mag. A*, 1998, **77**(4), 1013–1025.

48 H. Heinke, V. Kirchner, S. Einfeldt and D. Hommel, X-Ray Diffraction Analysis of the Defect Structure in Epitaxial GaN, *Appl. Phys. Lett.*, 2000, **77**(14), 2145–2147.

49 B. Moran, F. Wu, A. E. Romanov, U. K. Mishra, S. P. Denbaars and J. S. Speck, Structural and Morphological Evolution of GaN Grown by Metalorganic Chemical Vapor Deposition on SiC Substrates Using an AlN Initial Layer, *J. Cryst. Growth*, 2004, **273**(1–2), 38–47.

50 H. Heinke, V. Kirchner, S. Einfeldt and D. Hommel, Analysis of the Defect Structure of Epitaxial GaN, *Phys. Status Solidi A*, 1999, **176**(1), 391–395.